

Article

Application of Cold Metal Transfer Welding for High Pressure Die Casting Mold Restoration

Janette Brezinová¹, Miroslav Džupon², Marek Vojtko², Ján Viňáš¹, Ondrej Milkovič^{2,3}, Jakub Brezina¹, Anna Guzanová^{1,*} and Dagmar Draganovská¹ 

¹ Department of Engineering Technologies and Materials, Faculty of Mechanical Engineering, Technical University of Košice, Mäsiarska 74, 040 01 Košice, Slovakia; janette.brezinova@tuke.sk (J.B.); jan.vinas@tuke.sk (J.V.); jakub.brezina@tuke.sk (J.B.); dagmar.draganovska@tuke.sk (D.D.)

² Institute of Materials Research, Slovak Academy of Sciences, Watsonova 47, 040 01 Košice, Slovakia; mdzupon@saske.sk (M.D.); mvojtko@saske.sk (M.V.); omilkovic@saske.sk (O.M.)

³ Institute of Materials and Quality Engineering, Faculty of Materials, Metallurgy and Recycling, Technical University of Košice, Park Komenského 11, 040 01 Košice, Slovakia

* Correspondence: anna.guzanova@tuke.sk; Tel.: +421-55-602-3515

Received: 11 October 2019; Accepted: 14 November 2019; Published: 18 November 2019



Abstract: This paper presents results of the research focused on the possibility of the restoration of the shape parts of molds made of X15CrNiSi20-12 (EN 100 95) heat-resistant austenitic chromium-nickel stainless steel working in high-pressure die casting of aluminum alloys by clad welding. There were tested two welding wires—E Ni 6625 and E 18 8 Mn B 2 2—deposited on X15CrNiSi20-12 (EN 100 95) tool steel using cold metal transfer (CMT) welding in a protective atmosphere of Ar. The resistance of welds was tested against dissolution in molten aluminum alloy ENAC-AlSi9 and the testing procedure was designed. The resistance of welds against dissolution were assessed by exposition of welded clads in an aluminum melt for 120 and 300 min. The EDX semi-quantitative microanalyses of element distribution were performed at the welding–melt interface, and build-ups were also observed on the surface of welded clads.

Keywords: high-pressure die casting; dissolution; CMT welding

1. Introduction

High-pressure die casting technology (HPDC) is a balanced system of interrelations between the properties of the aluminum alloy melt, the design of the mold—including the inlet and venting, as well as the conditions of mold cavity filling, in particular the melt velocity in the mold—and the hydrodynamic pressure [1]. A key component of this technology is the mold and, mainly, its shape part—the mold insert. The morphology and microgeometry of the surface of the mold shape part is reflected in the surface quality of the aluminum castings. The particularity of HPDC technology is the mass production of thin-walled castings with a high quality of their surface.

Shape mold parts and mold cores for the casting of aluminum alloys must possess suitable physical and mechanical properties at elevated temperatures. These properties are essentially defined by the thermal and mechanical stresses as well as by the interaction at the interface between the mold and the aluminum alloy melt. In particular, the high velocities of the turbulent to dispersive filling of the mold cavity by the aluminum alloy melt, the high hydrodynamic pressures generated by the melt on the shape part of the mold and relatively high temperatures on the surface of shape parts of molds can significantly shorten the lifespan of molds and cores. All these phenomena cause the degradation of the surface of mold shape parts by mechanisms of erosion, abrasion, corrosion and heat fatigue of the mold, each of which act at the same time [2].

Since molds and dies work under heavy mechanical and thermal conditions, they are made of complex alloyed steels with the main alloying elements being Cr, V, Mo, or W, or a combination of these. Detailed analysis of the wear of different types of molds and dies was performed by Jhavar [3]. As the main mechanisms of mold damage, they identified wear (abrasive, adhesive, according to the purpose of the mold: mold for casting or die forging), erosion and mechanical and thermal fatigue. Jhavar [3] identified wear-influencing factors as follows: temperature, atmosphere, contact area, load, material properties, finish, velocity, lubrication, shape, vibration, sliding distance and type of motion. The material characteristics of molds and dies are also important, especially hardness, yield strength, elastic modulus, ductility, toughness, work-hardening characteristics, fracture toughness, microstructure, corrosion resistance, and in case of molds and dies in high-pressure die casting also resistance against solution in the melt [3].

Abrasive wear can occur in high-pressure casting molds due to insufficient mold cleaning between injection molding cycles in the area of the fitting surfaces between the mold parts. During this process, solidified particles of cast metal can act as abrasive particles. Depending on the shape and hardness of these particles, one of the following mechanisms of abrasive damage can occur: ploughing, cutting or fragmentation.

Adhesive wear of molds may occur in the event of insufficient lubrication and at high temperatures and friction rates. This results in an increase in the roughness of the mold surface and deterioration of the casting quality and process efficiency. The solubility of the mold material in the melt may also contribute to this. At high friction speeds in the presence of oxygen, oxidation of the mold material may also occur.

Thermal fatigue results from the cyclic change in the temperature of the functional mold surface relative to the material temperature next to the mold surface. These changes cause thermal stresses and lead to the formation of a network of cracks. Chander [4] and Chen [5] developed a thorough analysis of the thermal fatigue and identified the factors that affect it. They have been divided to die temperature cycle-related factors (preheating temperature, surface temperature of the die, holding time at peak temperature, cooling rate), basic die material properties' factors (thermal expansion coefficient, thermal conductivity, hot yield strength, temper resistance, creep strength, ductility) and to stress raisers' factors (fillets, holes and corners, surface roughness). Examples of high-pressure die damage after a certain lifetime period are shown in Figure 1.

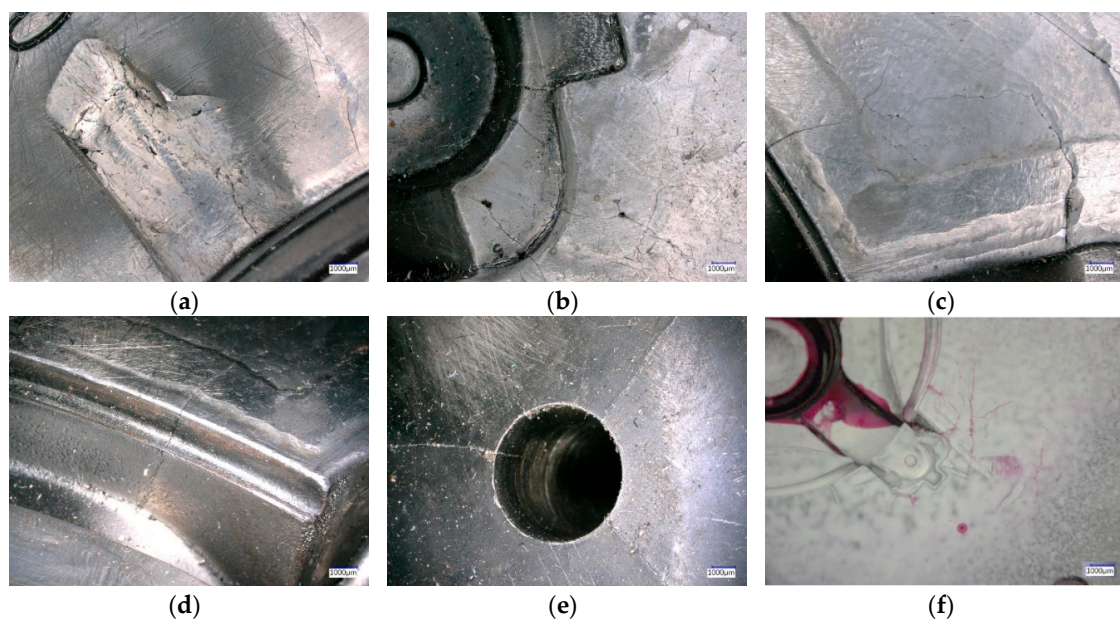


Figure 1. (a–f) Detail of damage on different locations of the surface of high-pressure casting die after 800,000 working cycles.

Typically, the different types of wear occur in combination, interact and contribute to the resulting complex wear, while the prevailing wear mechanism can vary in the different phases of mold life. However, the resulting wear will also be affected by the solubility of the mold material in the melt. The dissolution of the mold material in the melt is prevented by the application of thin coatings on the functional surface of the mold by PVD or PE-CVD technology, but during operation these coatings may also be locally damaged and worn.

According to Chander [3], mold production costs may account for up to 30% of the total production costs per product. According to Chen [5] up to 80% of the molds for automotive components have undergone renovation. Therefore, the topic of finding suitable ways of repairing and renovating molds is highly relevant.

In order to ensure the longest possible life for the die and detect the early stages of wear, it is necessary to regularly check the extent of mold damage. Since mold materials are mostly high-alloy steels with a higher carbon content, which means low weldability, a suitable technology for refilling worn material needs to be considered [6]. The philosophy of the architecture of welded clads designated for the restoration of HPDC molds requires the following conditions to be met: (a) the weld must be chemically inert towards the aluminum melt; (b) the welding must have specific mechanical, chemical and physical properties defined by the HPCD process, i.e., the weld must be resistant to wear and oxidation; (c) the weld must compensate for the thermal and residual stresses generated by the HPDC process; (d) the weld must have good adhesion to the substrates; and (e) the weld must be able to delay the thermal fatigue [7–9].

Among the different deposition techniques, the fusion welding technologies (GTA—gas tungsten arc welding PTAW—plasma transferred arc welding, micro-GTAW, microplasma, laser powder deposition, EBW—electron beam welding, TIG—tungsten-electrode inert gas welding) are main welding techniques utilised in mold restoration [10]. Especially, laser cladding is a frequent topic of research [11–14].

During fusion welding, the metallurgical relationship between the base metal (BM) and deposited material varies with respect to time, volume and the pattern of deposition. As the different deposition process leads to different cooling rates, different sets of microstructures and residual stress states [13,14] form. At high cooling rates (laser, plasma and EBW) austenite fully transforms into martensite. At lower cooling rates (GTAW), ferrite and pearlite are formed. At medium cooling rates, microstructures consisting of ferrite, pearlite, bainite and martensite are produced. Thus, various deposition techniques give rise to the formation of different material properties leading to different die and mold life. The post repairing life of dies and molds depends on the quality of repair, in addition with pre and post repair heat-treatments [4].

One of the possibilities of restoring functional surfaces of injection molds or coremakers is with arc welding by CMT (cold metal transfer). Damaged parts of the molds are machined and, consequently, the layers are welded and deposited on these surfaces. Molds renovated this way are heat-treated and machined to the required dimensions and surface quality. The latest published research on mold restoration by welding [5,6,15–18] aims to identify ways and possibilities to increase mold surface lifetime using CMT welding and to verify the suitability of the chemical composition of newly developed additive materials for mold restoration. Such layers will withstand the presented combinations of tribodegradation factors while being resistant to the action of the injected liquid.

Cold metal transfer technology has revolutionized welding of both similar and dissimilar metals for thick-sectioned components by producing improved weld bead aesthetics with controlled metal deposition and low heat input.

Selvi [19] provided a detailed description of the CMT process. In the CMT process, as soon as the electrode makes contact with the molten pool, the welding torch is reversed, causing the wire to retract, promoting droplet transfer. During metal transfer, the current drops to near-zero and thereby any spatter generation is avoided. When the metal transfer is completed, the arc is re-ignited and the wire is fed forward once more with set welding current reflowing. The procedure is continually

repeated and automated [20]. Selvi [19] further analysed the metallography and metallurgy of joints created by CMT welding both for similar and dissimilar materials. Welding dissimilar materials with different melting temperatures results in the welding process being defined as a soldering technique, characterized by a narrow diffusion zone containing intermetallic phases.

Pang and Cong et al. [18,21] investigated the influence of the heat input in CMT and modified the CMT welding process (CMT-pulsed, CMT-advanced, CMT-pulse advanced) to optimize the weld bead geometry and minimize porosity. Chen [17] studied CMT welding of mild steel under different welding conditions and the effect of cold metal transfer on the final weld geometry and weld quality. A combination of laser-CMT, TIG-CMT [22], or the CMT method assisted with a hybrid magnetic field can also be used [23].

The aim of the work is to verify the use of E Ni 6625, E 18 8 Mn B 2 2 materials (welding wires) on high-pressure casting die restoration from the point of view of their resistance to solubility in an ENAC- AlSi_9 aluminum alloy melt. The ambition of the authors is also to design an effective method of evaluating the welded clads' resistance against dissolution in an Al-based melt for a better qualitative evaluation of welded clads used for the renovation of shaped parts of molds for the HPDC processes.

2. Materials and Methods

E Ni 6625 (EN ISO 14172) and E 18 8 Mn B 2 2 (EN ISO 3581-A) welds were deposited on steel plates with a thickness of 10 mm made of the base metal (X15CrNiSi20-12—EN 100 95) stainless steel using welding equipment Fronius Trans Puls Synergic 5000 by CMT (Fronius International GmbH, Wels, Austria) in an argon protective atmosphere (Figure 2). The welding parameters were: 155 A, 16.5 V, $8.5 \text{ m}\cdot\text{min}^{-1}$ with a wire feed of $8 \text{ m}\cdot\text{min}^{-1}$. The chemical composition of the BM and the two wires used E Ni 6625 and E 18 8 Mn B 2 2 were analysed using a Belec Compact Port spectral chemical analyser (Belec Spektrometrie Opto-Elektronik GmbH, Georgsmarienhütte, Germany). The corresponding chemical compositions are shown in Table 1. Mechanical properties of used materials given by the material producer are shown in Table 2.



Figure 2. Fronius Trans Pulse Synergic 5000 CMT.

Table 1. Chemical composition of used materials (wt%). Bal.—balance.

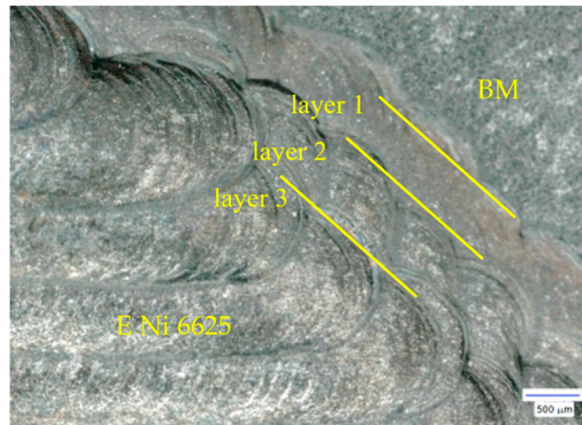
Material	C	Mn	Si	Cr	V	Mo	Nb	Cu	Ni	Ti	Co	Fe
BM	0.075	0.408	1.153	19.48	0.058	0.071	-	0.079	13.92	0.011	0.035	Bal.
E Ni 6625	0.004	0.855	0.562	20.42	0.006	8.13	3.1	-	Bal.	0.004	0.004	0.9
E 18 8 Mn B 2 2	0.101	7.915	0.838	18.81	0.084	0.020	-	0.052	9.85	0.005	0.056	Bal.

Table 2. Mechanical properties of used materials (average values) provided by producer *.

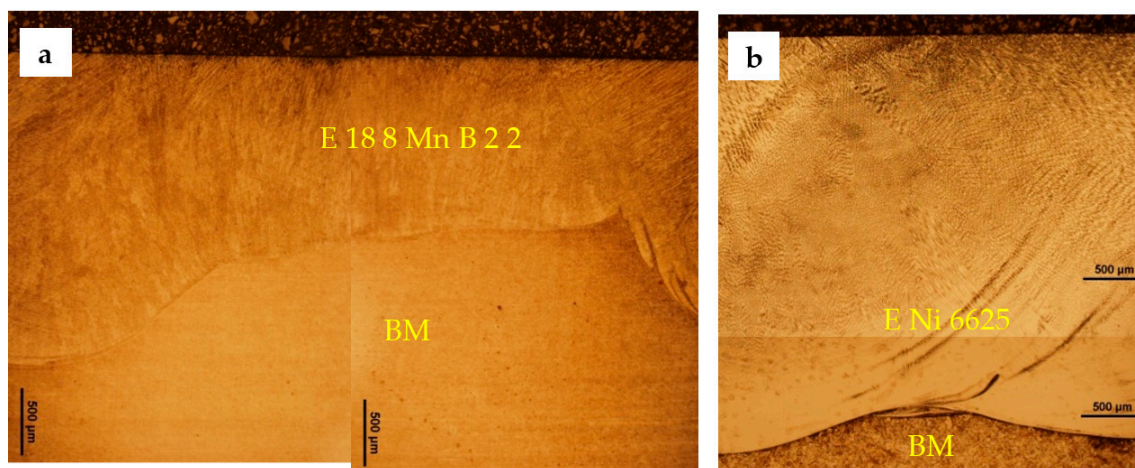
Material	Yield Strength $R_{p0.2}$ (MPa)	Ultimate Tensile Strength R_m (MPa)	Elongation A_5 (%)
BM	260	750	30
E Ni 6625	420	760	30
E 18 8 Mn B 2 2	350	600	40

* Voestalpine Böhler Welding.

The appearance of the surface with the E Ni 6625 layer deposited is shown Figure 3.

**Figure 3.** The appearance of the surface of the three-layer CMT welded clad E Ni 6625.

Observing metallographic cross-sections of three-layer welded clads of E 18 8 Mn B 2 2 and E Ni 6625 deposited on BM (Figure 4a,b) by means of light microscope, no cracks, cavities, clowholes, macroscopic and microscopic pores, various inclusions and fusion defects in the weld area and between individual welded layers were detected.

**Figure 4.** Three-layer welded clads of (a) E 18 8 Mn B 2 2 and (b) E Ni 6625 deposited on the BM.

Immersion Test

In order to simulate real operating conditions, the weld resistance against dissolution was assessed in immersion in the aluminum alloy ENAC-AISi9 melt. For the stated tests, samples of E Ni 6625 and E 18 8 Mn B 2 2 with dimensions of 20 mm × 20 mm × 10 mm were taken from a parent plate, where the weld deposit was on one side of the sample while the other side of the sample represented the

base material. The test specimens prepared in this way made it possible to test the resistance of the weld and base material in the melt of ENAC- AlSi9 simultaneously and under the same conditions. The ENAC- AlSi9 alloy melt then reacted with the clad and base material at the same temperature, for the same time and with the same chemical composition as the ENAC- AlSi9 alloy melt. Such an experimental setup provided information on the relative resistance of the weld deposit and the base material against dissolution in the ENAC- AlSi9 alloy melt. The aluminum alloy melt was prepared from portions of AlSi9 aluminum alloy, which were embedded into ceramic crucibles and heated in a laboratory furnace to the melting point of the alloy. The temperature of the alloy was maintained at 680 ± 20 °C, which is the casting temperature of ENAC- AlSi9 alloy in pressurized casting on machines with cold filling chambers. All test samples were fastened in the vertical position and completely immersed in a still melt in ceramic crucibles. Test samples were exposed to the aluminum alloy melt for 120 and 300 min, then removed from the melt and cooled freely in still air. On both surfaces of the samples solid aluminum alloy remained.

Samples intended for analyses using light and scanning electron microscopes were taken from experimental clads by electrospark machining, mounted in conductive dentacryle, wet grinded on a set of abrasive papers of grit size # 240, 400, 600 and 800, polished using 0.9, 0.3 and 0.1 μm diamond emulsions on appropriate bases, and washed and rinsed with alcohol. The microstructure of the welded clads and base material were highlighted by etching in the following etching agents: E 18 8 Mn B 2 2—120 mL CH_3COOH , 20 mL HCl , 3 g picric acid, 144 mL CH_3OH , E Ni 6625—5 mL HNO_3 , 25 mL HCl and 30 mL distilled water, base material BM—1 g picric acid, 5 mL HCl , 97 mL ethyl alcohol. Microstructures were observed using and OLYMPUS GX71 light optical microscope (OLYMPUS Europa Holding GmbH, Hamburg, Germany). Prior to observation, samples underwent ultrasonic cleaning in methanol. For material quality assessment, EDX microanalyses of element distribution at the interface between welded clads or BM and ENAC AlSi9 melt after exposure, a SEM EVO MA15 environmental scanning electron microscope (Carl Zeiss, Jena, Germany) with integrated analytical units EDX and WDX (Oxford Instruments, Abingdon, UK) was used. For SEM analyses, regime SEI (secondary electron) with an accelerating voltage of 20 kV and a distance from the sample surface of 10 mm and BSE (backscattered electron) regime, allowing the observation of chemical contrast were used.

Diffraction measurements were performed on a Philips X'Pert PRO MDP (PANalytical Inc., Almelo, the Netherlands) device using Cu radiation. The acquisition time of each sample was 42.8 min. The phase composition of the samples was determined using the PDF2 database and the subsequent Rietveld structure refinement was performed using MAUD software (version 2.92 (29.07.2019), Trento, Italy) [24]. Hardness was measured using a Vickers 432 SVD hardness tester (Wolpert Wilson Instruments, Division of INSTRON DEUTSCHLAND GmbH, Aachen, Germany) at a load of 98.07 N for 15 s.

3. Results and Discussion

3.1. Microstructure Characterization

3.1.1. Microstructure of E Ni 6625 Welded Clad

Figure 5 shows the microstructure of the E Ni 6625 layer from the surface to the base material. In the upper and middle parts of the layer, columnar and coaxial dendritic microstructure were identified. The main axes of the dendrites were oriented in the direction of the maximum temperature gradient during solidification of the weld melt. Dendrites showed an uneven and random orientation during growth. The orientation of the growth dendrites suggests that heat was particularly conducted by the base material. The direction of heat flow at cooling was perpendicular to the surface of the base material, and as a result, directionally-oriented dendrites were formed. In the fusion zone, light and electron microscopy confirmed good metallurgical bonding of the weld deposit to the base material. During the CMT process, the individual layers of cladding are formed by a rapid solidification process

that begins with the formation of a continuous austenitic matrix based on the nickel-phase γ . The γ phase typically contains a high percentage of the elements forming substitute solid solutions, e.g., Cr, Mo [24,25].

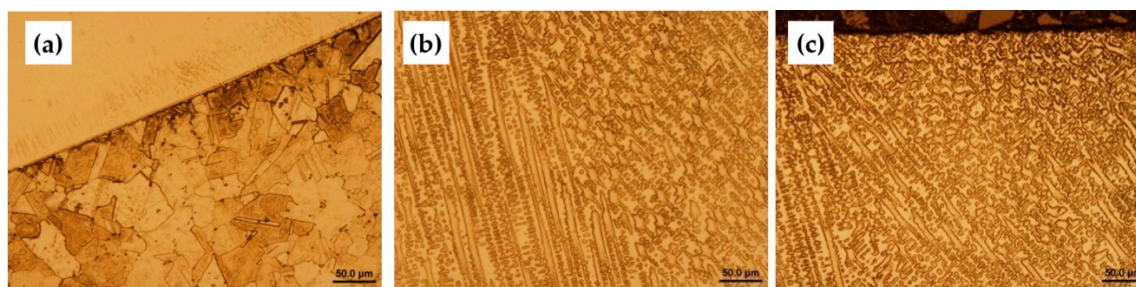


Figure 5. Microstructure of the three-layer CMT welded clad made using E Ni 6625, (a) fusion zone, (b) middle part, and (c) surface of the clad.

At the bottom of the E Ni 6625 clad, at the fusion zone, the iron concentration was increased as a result of intensive mixing of the base material with the weld clad (Figure 6, Table 3). Elements present in BM steel were detected by local EDX microanalysis in the BM (Table 3). In a fusion zone of thickness of 3–4 μm , molybdenum and silicon were present in the iron matrix in addition to the chromium alloy (Table 3).

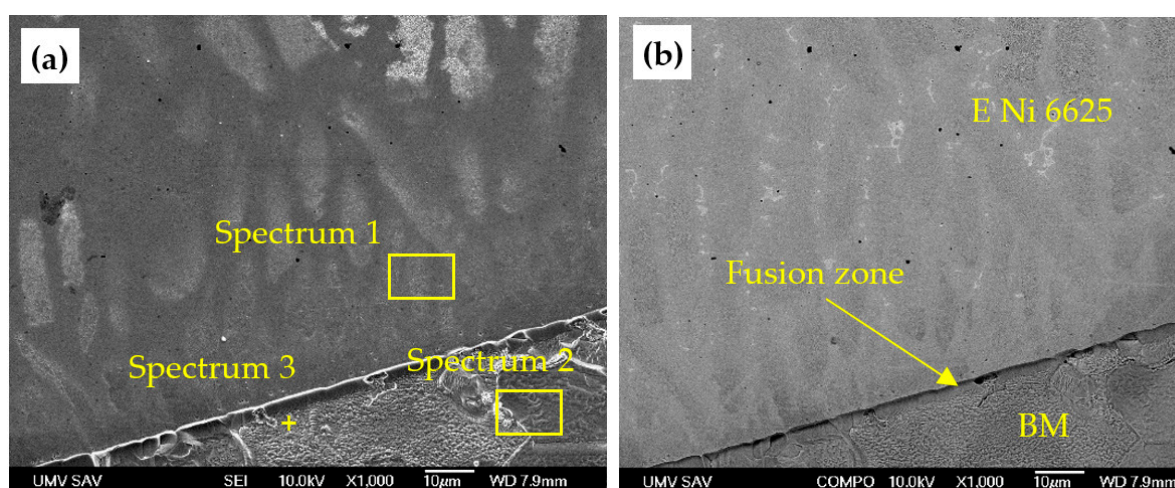


Figure 6. E Ni 6625/BM, semi-quantitative EXD microanalysis of the fusion zone (a), and the fusion zone, SEM-BSE (b).

Table 3. EDX analysis of spectra 1–3, wt.%.

Element	Spectrum 1	Spectrum 2	Spectrum 3
Cr K	21.05	17.41	20.68
Fe K	27.91	68.40	77.96
Ni K	46.40	12.69	-
Mo L	4.64	-	0.77
Si K	-	1.51	0.60
Totals	100.00	100.00	100.00

E Ni 6625 is a nickel-based superalloy strengthened with alloying elements such as Cr and Mo, which primarily cause substitution strengthening of austenitic microstructures. For Nb-containing alloys, secondary phases are formed in the interdendritic region. The presence of other alloying elements reduces the solubility of Nb and Mo in nickel. When a drop of melt solidifies, γ phase

dendrites are formed immediately and the remaining melt is enriched with Nb and Mo. Due to dendritic segregation at the dendrite-melt boundary, interdendritic areas are enriched with Nb and Mo [26,27]. Reallocation of alloying elements was observed in the central part of the weld deposit as well as on its surface (Figure 7, Tables 4 and 5).

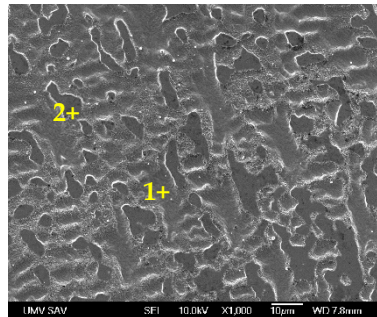


Figure 7. E Ni 6625, central part of the weld deposit, semi-quantitative EDX microanalysis.

Table 4. EDX, spectrum 1.

Element	Weight%
Cr K	19.02
Fe K	9.74
Ni K	64.77
Mo L	6.46
Totals	100.00

Table 5. EDX, spectrum 2.

Element	Weight%
Cr K	16.90
Fe K	7.36
Ni K	52.08
Nb L	15.57
Mo L	8.09
Totals	100.00

Information on the distribution of alloying elements in Tables 4 and 5 in the E Ni 6625 weld were obtained by the EDX surface and point microanalyses of welds, mixing zone and base material. The distribution of alloying elements in E Ni 6625 welds before immersion in the aluminium alloy melt was uniform with no locally-increased concentration (Figure 8).

3.1.2. Microstructure of E 18 8 Mn B 2 2 Welded Clad

Figure 9a shows the original austenitic microstructure of the BM substrate and the fusion zone of E 18 8 Mn B 2 2 welded clad. The microstructure of the deposit mainly consisted of the austenitic matrix and the skeleton form of delta ferrite (Figure 9b,c). This type of microstructure arose as a result of the solidification way of E 18 8 Mn B 2 2 and depended on the equivalent chromium $[Cr]_{eq}$ to equivalent nickel $[Ni]_{eq}$ ratio [28].

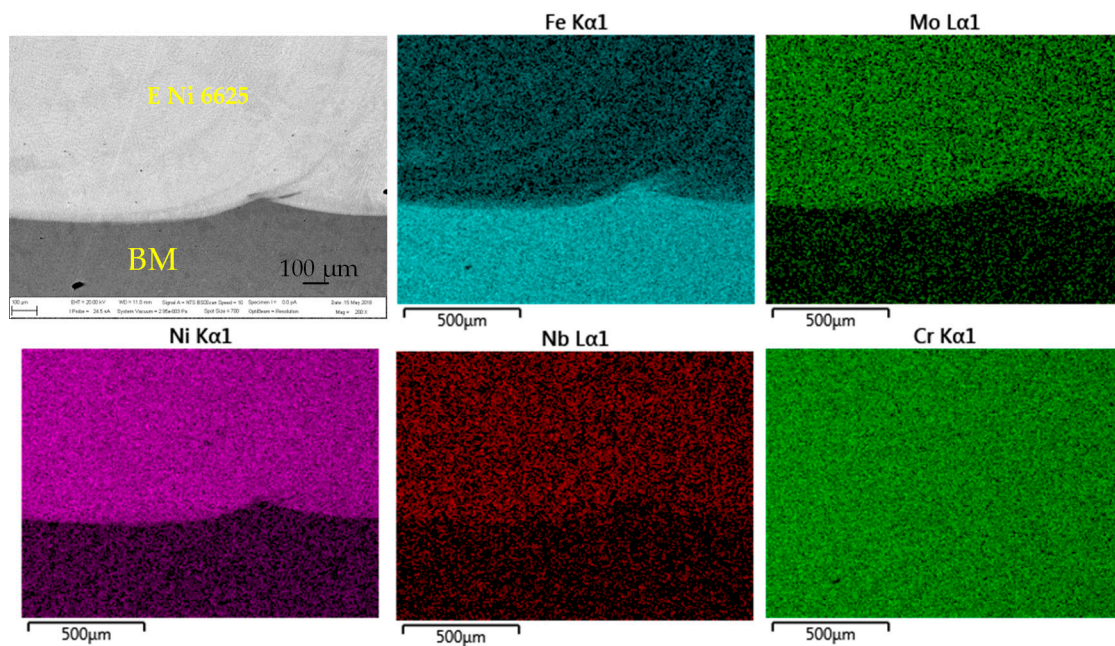


Figure 8. E Ni 6625 weld—EDX semi-quantitative microanalyses (mapping).

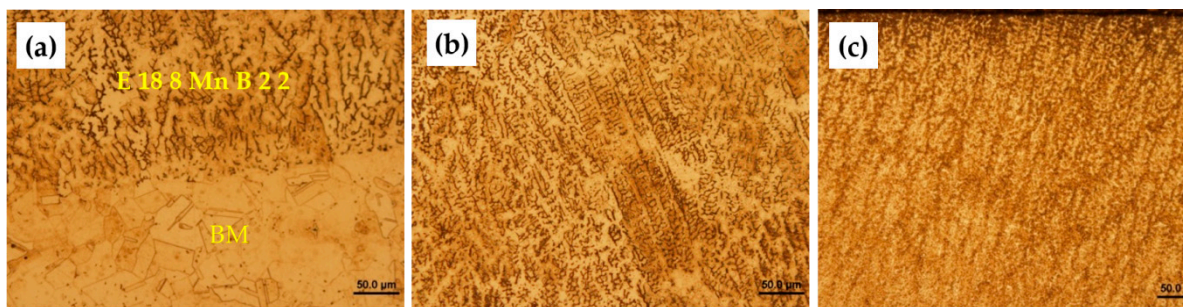


Figure 9. Microstructure of the three-layer CMT weld clad made using E 18 8 Mn B 2 2: fusion zone (a), middle part (b) and surface of the clad (c).

Intensive mixing of the weld metal during the welding process and locally different solidification rates of the weld metal were a potential source of local heterogeneities in the chemical composition of the weld deposit [29,30].

The concentrations of Cr, Ni and Mn corresponded to the values for the base material and E 18 8 Mn B 2 2. EDX mapping showed no heterogeneity in the distribution of Mn, Cr and Ni alloys in the fusion zone and in the weld deposit. Distribution of alloying elements in E 18 8 Mn B 2 2 welds before immersion in the aluminum alloy melt was uniform with no locally-increased concentration (Figure 10).

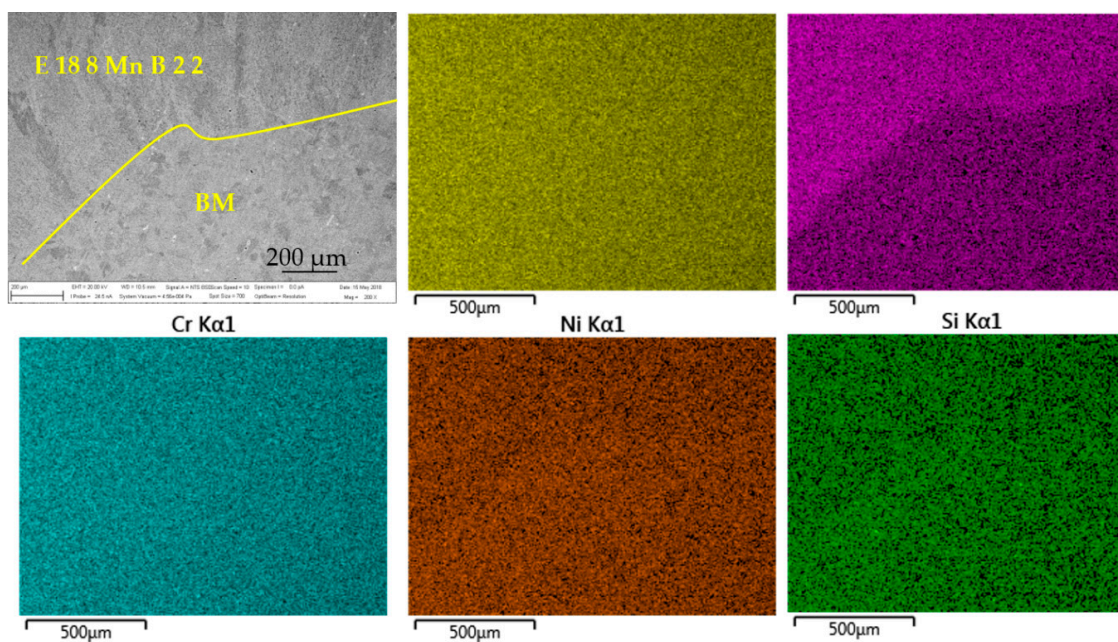


Figure 10. E 18 8 Mn B 2 2 welded clad—EDX semi-quantitative microanalyses (mapping).

Figure 11 and Table 6 show the results of the phase analysis of welded clads. Figure 11a shows a refined diffraction spectrum of E Ni 6625. One phase with a spatial group $Fm\bar{3}m$ was identified that corresponds to the austenitic phase in the weld deposit. The parameters are shown in Table 6. Figure 11b shows a fitted diffraction spectrum of E 18 8 Mn B 2 2.

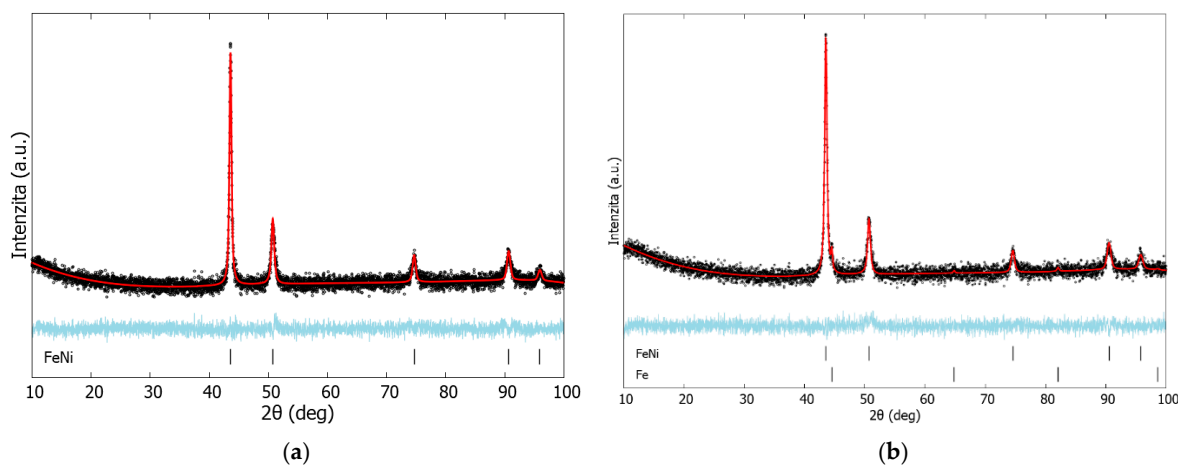


Figure 11. Diffraction spectrum: E Ni 6625 (a), E 18 8 Mn B 2 2 (b).

Table 6. Parameters from refining diffraction spectra.

Materials	a_{FeNi} (Å)	a_{Fe} (Å)	FeNi (wt.%)	Fe (wt.%)	σ	R_{wp} (%)
E 18 8 Mn B 2 2	3.5961	2.8735	94.8	5.2	1.2	2.76
E Ni 6625	3.5922	-	100	-	1.22	2.89

Two phases have been identified in welded clads. The majority phase is the same as for E Ni 6625. The minority phase will need to be dealt with in more detail because there was not a sufficient signal of weaker reflections to identify it. For fitting the structure, the phase $Im\bar{3}m$ corresponding to the α -Fe phase was used. Output fitted parameters are also shown in Table 6.

The hardness of the E 18 8 Mn B 2 2 and E Ni 6625 deposited on the BM was measured in the weld metal, the fusion zone and the heat-affected zone of the base material (Figure 12).

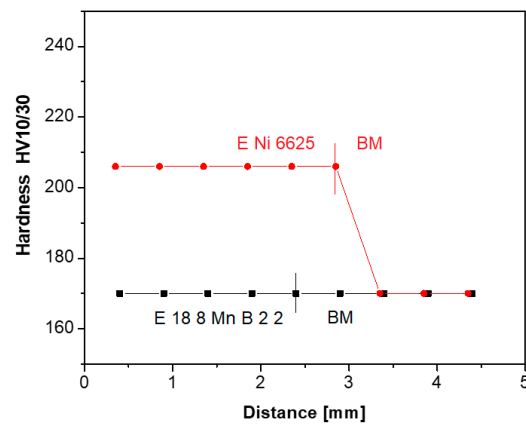


Figure 12. Hardness of the welded clads.

A hardness of 170 HV10/30 was measured in the E 18 8 Mn B 2 2, in the fusion zone and in the base material. The hardness of the E Ni 6625 deposit was 207 HV10/30, and the hardness of the base material was 170 HV10/30.

3.2. Immersion Test

3.2.1. Immersion Test of E Ni 6625

The resistance of E Ni 6625 welds on the base material of BM quality was tested by complete immersion in the ENAC-AlSi9 aluminum alloy melt maintained at a temperature of 680 ± 20 °C in a laboratory resistance furnace for 120 and 300 min (Figures 13 and 14). When the welded clad is immersed in the melt at temperature of 680 ± 20 °C, dissolution reactions at the clad–melt boundary, mass transfer to the melt or mass transfer from the melt to the clad–melt boundary and precipitation and recrystallization processes continuously occur in the melt [31–33]. The microstructure and composition of intermetallic compounds in the system E Ni 6625 and ENAC-AlSi9 melt was studied on test samples with the weld deposit following the methodology mentioned in Section 2.

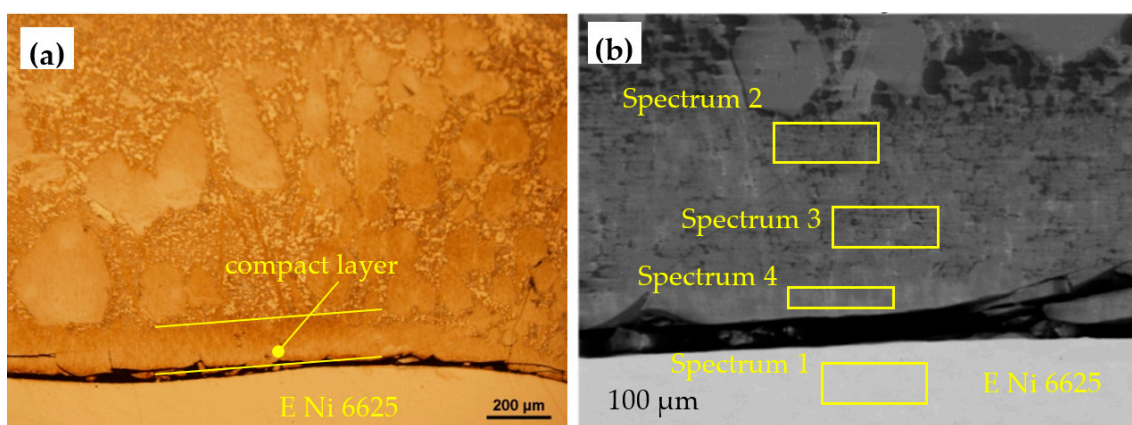


Figure 13. E Ni 6625/680 °C/120 min/AlSi9. Intermetallic compounds at the boundary between the E Ni 6625 deposit and the solidified aluminum alloy melt (a). EDX semi-quantitative microanalyses (b).

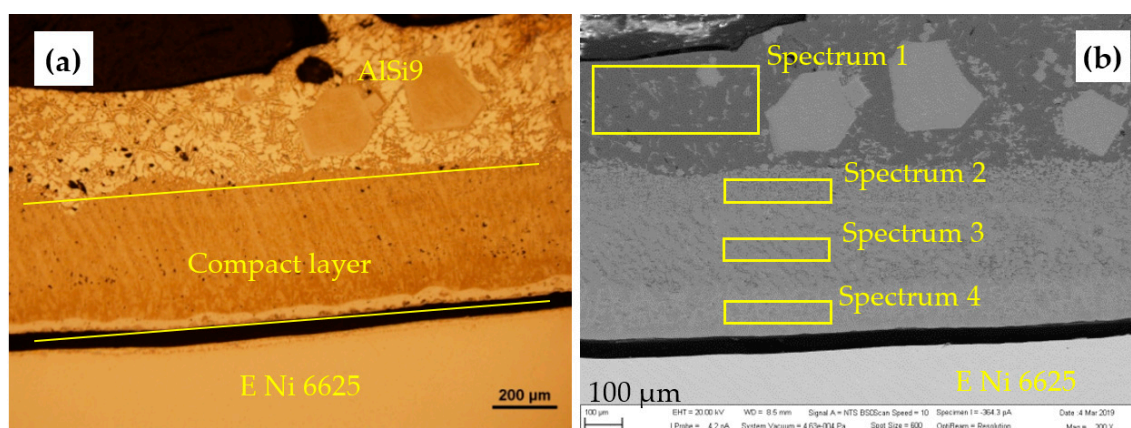


Figure 14. E Ni 6625/680 °C/300 min/AlSi9. Intermetallic compounds at the boundary between the E Ni 6625 deposit and the solidified aluminum alloy melt (a). EDX semi-quantitative microanalyses (b).

After 120 min exposure in the melt, a layered structure of intermetallic compounds arose at the boundary of the E Ni 6625 weld deposit and the solidified melt of the aluminum alloy. There was a compact layer in the solidified melt zone of the aluminum alloy, closely adjacent to the E Ni 6625 deposit in which Al, Si, Fe, Cr, Mo and Ni were detected. At the boundary of the E Ni 6625 deposit and the solidified aluminum alloy melt, there was a higher nickel concentration than in the rest of the layer (Figure 15, Table 7).

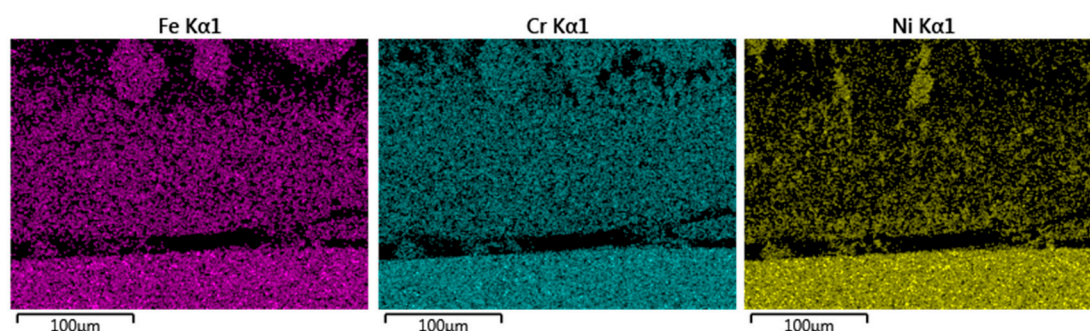


Figure 15. E Ni 6625/680 ± 20 °C/120 min/AlSi9. EDX semi-quantitative microanalyses (mapping).

Table 7. E Ni 6625/680 ± 20 °C/120 min/AlSi9 EDX semi-quantitative microanalyses.

	Spectrum 1		Spectrum 2		Spectrum 3		Spectrum 4	
Elemt	Weight%	Weight%	Weight%	Weight%	Weight%	Weight%	Weight%	
Al	-	53.12	53.02	46.94				
Si	0.41	12.31	11.53	11.55				
Cr	22.4	13.29	13.52	12.11				
Fe	13.51	7.66	8.14	8.58				
Ni	53.08	7.71	8.57	14.61				
Mo	7.45	4.16	3.98	4.15				
Nb	2.94	1.75	1.24	1.7				
Ti	0.21	-	-	0.36				
Totals	100.00	100.00	100.00	100.00				

The resistance of E Ni 6625 welded clad against dissolution after immersion time 300 min in ENAC-AlSi9 alloy was analysed in the same way. After immersion in the melt, a massive layered intermetallic compound structure was formed at the boundary of the E Ni 6625 welded clad and the solidified melt. A compact layer based on Al-Si-Fe-Cr-Mo-Ni was contained in the solidified melt

of the aluminum alloy adjacent to the E Ni 6625 clad. At the boundary of the solidified melt of the aluminum alloy and the E Ni 6625 weld deposit, the concentration of Ni and Fe in the compact layer was increased relative to the rest of the layer. The concentration of Cr and Fe was approximately half that of the weld deposit (Figures 15–17, Table 8).

Qualitative areal and line microanalysis provided information on the distribution of Fe, Cr and Ni in a compact layer on the boundary of the E Ni 6625 clad and the solidified aluminum melt (Figures 16 and 17).

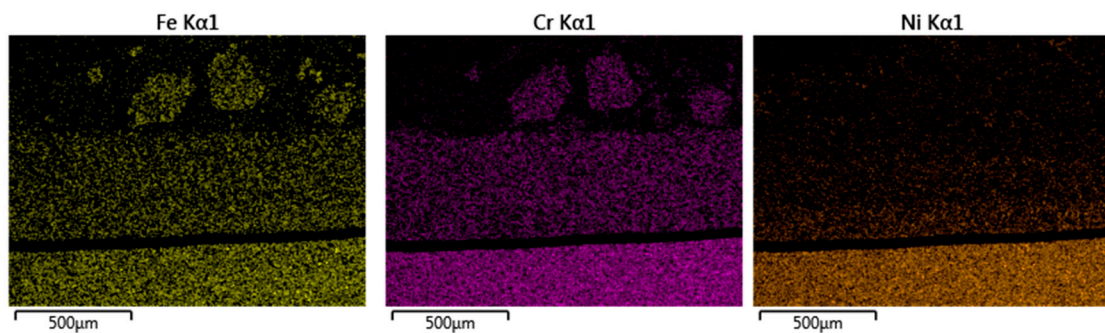


Figure 16. E Ni 6625/680 ± 20 °C/300 min/AlSi9. EDX semi-quantitative microanalyses (mapping).

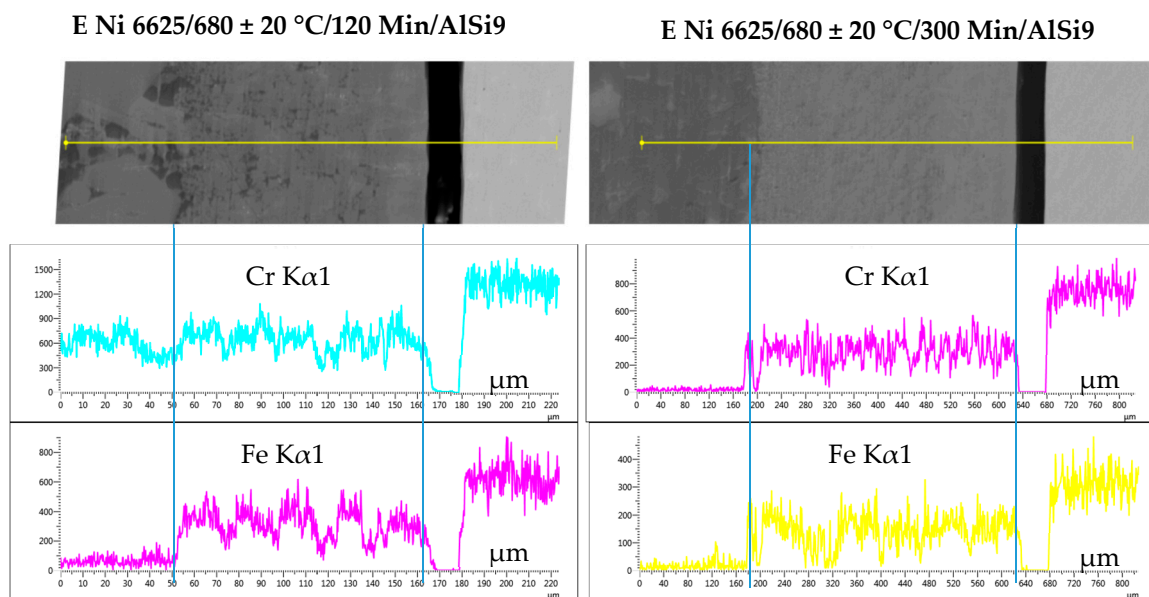


Figure 17. EDX line microanalysis.

Table 8. E Ni 6625/680 ± 20 °C/300 min/AlSi9. EDX semi-quantitative microanalyses.

	Spectrum 1	Spectrum 2	Spectrum 3	Spectrum 4
Element	Weight%	Weight%	Weight%	Weight%
Al	79.46	57	55.17	49.42
Si	15.98	15.93	11.68	10.65
Cr	0.64	11.82	11.99	10.43
Fe	1.14	6.02	7.61	8.15
Ni	2.78	3.65	7.97	16.16
Mo	-	3.9	3.96	3.44
Nb	-	1.69	1.39	1.44
Ti	-	-	0.22	-
Mn	-	-	-	0.31
Totals	100.00	100.00	100.00	100.00

In a mixture of solidified melt of AlSi9 alloy, corrosion products of the melt with E Ni 6625, intermetallic compounds were observed as layered structures or isolated blocks in the liquid portion of the melt after solidification. Analogous observations have been made in [34–38]. Intermetallic compounds of NiAl₃, Ni₂Al₃, NiAl, Ni₅Al₃ and Ni₃Al types have been observed in the Ni–Al binary system at a temperature range of 550–900 °C. In all binary intermetallic compounds, the solubility of silicon, which was a substitute for aluminum, was limited [34,35].

The aim of analyses of the compact layer at the boundary of weld deposit and corrosion products coming from reaction between the melt and welded clads was to identify the thickness of the corrosion products which would be suitable for qualitative assessment of welded clad resistance to corrosion dissolution in the melt of aluminum alloy ENAC-AlSi9.

3.2.2. Immersion Test of E 18 8 Mn B 2 2

The resistance of E 18 8 Mn B 2 2 deposited on the base material of BM quality was tested by complete immersion in the aluminum alloy melt ENAC-AlSi9 maintained at a temperature of 680 ± 20 °C in a laboratory resistance furnace for 120 and 300 min. In both cases welds reacted with the aluminum alloy melt with different intensities (Figures 18 and 19, Table 9).

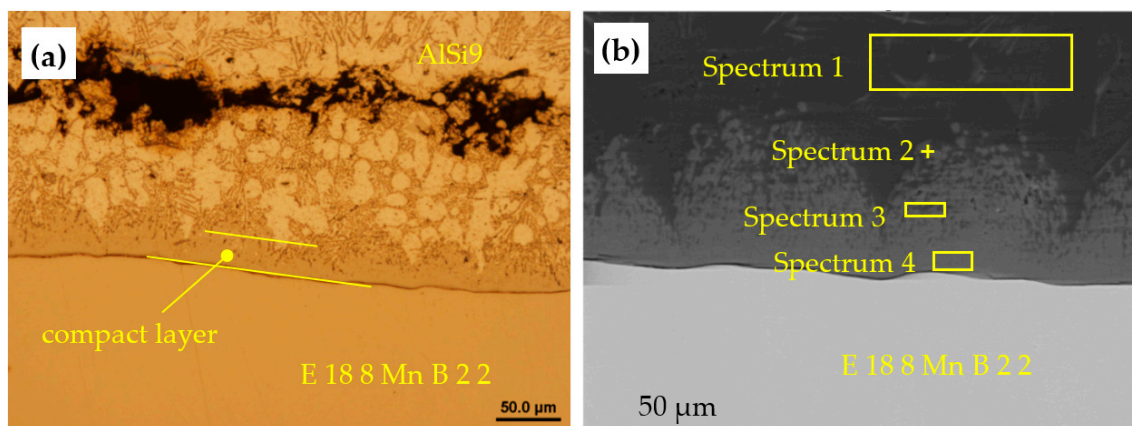


Figure 18. E 18 8 Mn B 2 2/ 680 ± 20 °C/300 min/AlSi9. Intermetallic compounds at the boundary between the E 18 8 Mn B 2 2 deposit and the solidified aluminum alloy melt (a). EDX semi-quantitative microanalyses (b).

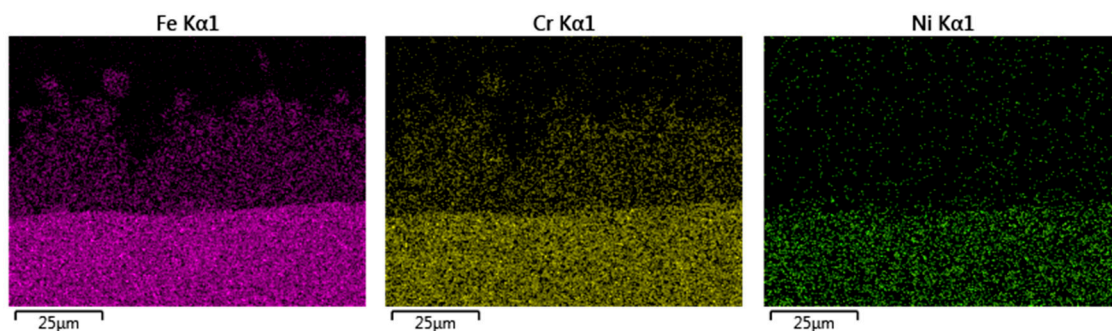


Figure 19. E 18 8 Mn B 2 2/ 680 ± 20 °C/120 min/AlSi9. EDX semi-quantitative microanalyses (mapping).

Table 9. E 18 8 Mn B 2 2/680 ± 20 °C/120 min/AlSi9. EDX semi-quantitative microanalyses.

	Spectrum 1		Spectrum 2	Spectrum 3	Spectrum 4
Elemt	Weight%	Weight%	Weight%	Weight%	Weight%
Al	88.92	58.57	58.66	57.50	
Si	9.66	16.37	9.22	8.41	
Cr	-	6.83	8.38	7.83	
Fe	1.42	16.94	22.05	24.76	
Mn	-	1.29	1.18	0.72	
Ni	-	-	0.52	0.78	
Totals	100.00	100.00	100.00	100.00	

After exposure of the E 18 8 Mn B 2 2 deposit for 120 min in the ENAC-AlSi9 melt, on the boundary between the E 18 8 Mn B 2 2 and the AlSi9 solidified melt, layered structure of intermetallic compounds was observed. In the solidified melt zone of the AlSi9 aluminum alloy adjacent to the E 18 8 Mn B 2 2 deposit, there was a compact layer of intermetallic compounds in which the elements Al, Si, Fe, Cr, Ni and Mn were detected.

Analogously, samples of E 18 8 Mn B 2 2 deposited on the BM base material were analysed after a 300 min immersion in AlSi9 alloy melt. After an exposure time of 300 min in the AlSi9 alloy melt, a massive layered intermetallic compound structure based on Al, Si, Fe and Cr was formed at the boundary of the E 18 8 Mn B 2 2 welded clad and the solidified melt (Figures 20 and 21, Table 10). The Cr concentration was approximately half that of the weld deposit.

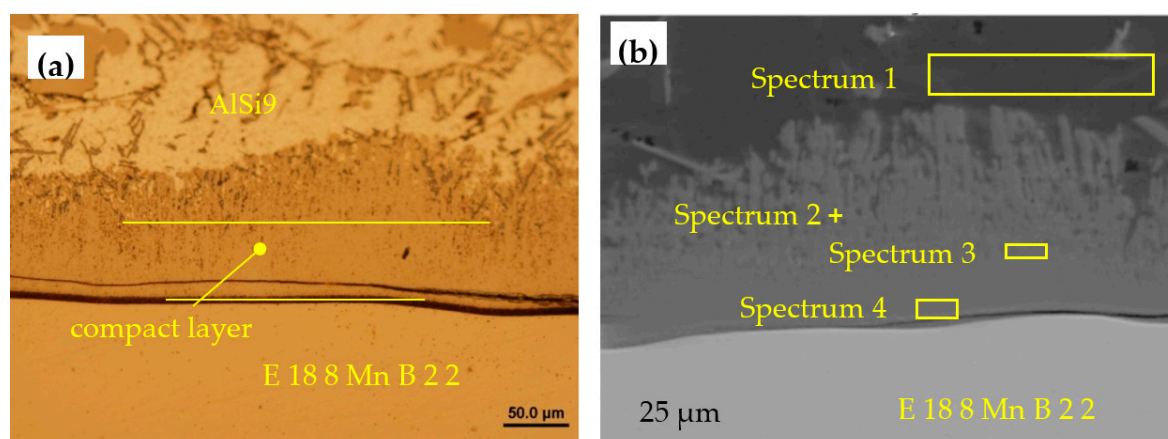


Figure 20. E 18 8 Mn B 2 2/680 ± 20 °C/300 min/AlSi9. Intermetallic compounds at boundary between the E 18 8 Mn B 2 2 deposit and the solidified aluminum alloy melt (a). EDX semi-quantitative microanalyses (b).

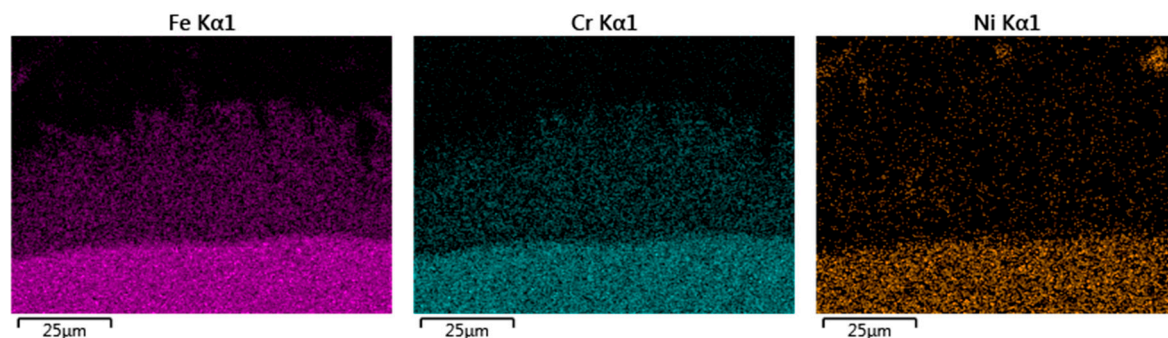


Figure 21. E 18 8 Mn B 2 2/680 ± 20 °C/300 min/AlSi9. EDX semi-quantitative microanalyses (mapping).

Table 10. E 18 8 Mn B 2 2/680 ± 20 °C/300 min/AlSi9. EDX semi-quantitative microanalyses.

	Spectrum 1		Spectrum 2	Spectrum 3	Spectrum 4
Elemt	Weight%	Weight%	Weight%	Weight%	Weight%
Al	85.70	63.22	58.05	50.19	50.19
Si	50.19	7.97	9.04	7.32	7.32
Cr	-	6.84	7.79	8.85	8.85
Fe	0.43	20.70	23.73	28.88	28.88
Mn	-	1.27	0.94	-	-
Ni	0.58	-	0.45	4.07	4.07
Totals	100.00	100.00	100.00	100.00	100.00

The uniform distribution of aluminum, iron, chromium and nickel was detected in the compact layer using the qualitative areal and line EDX microanalysis at the boundary of the E 18 8 Mn B 2 2 cladding and the solidified aluminum alloy melt ENAC-AlSi9, Figure 22.

E 18 8 Mn B 2 2/680 ± 20 °C/120 Min/AlSi9 **E 18 8 Mn B 2 2/680 ± 20 °C/300 Min/AlSi9**

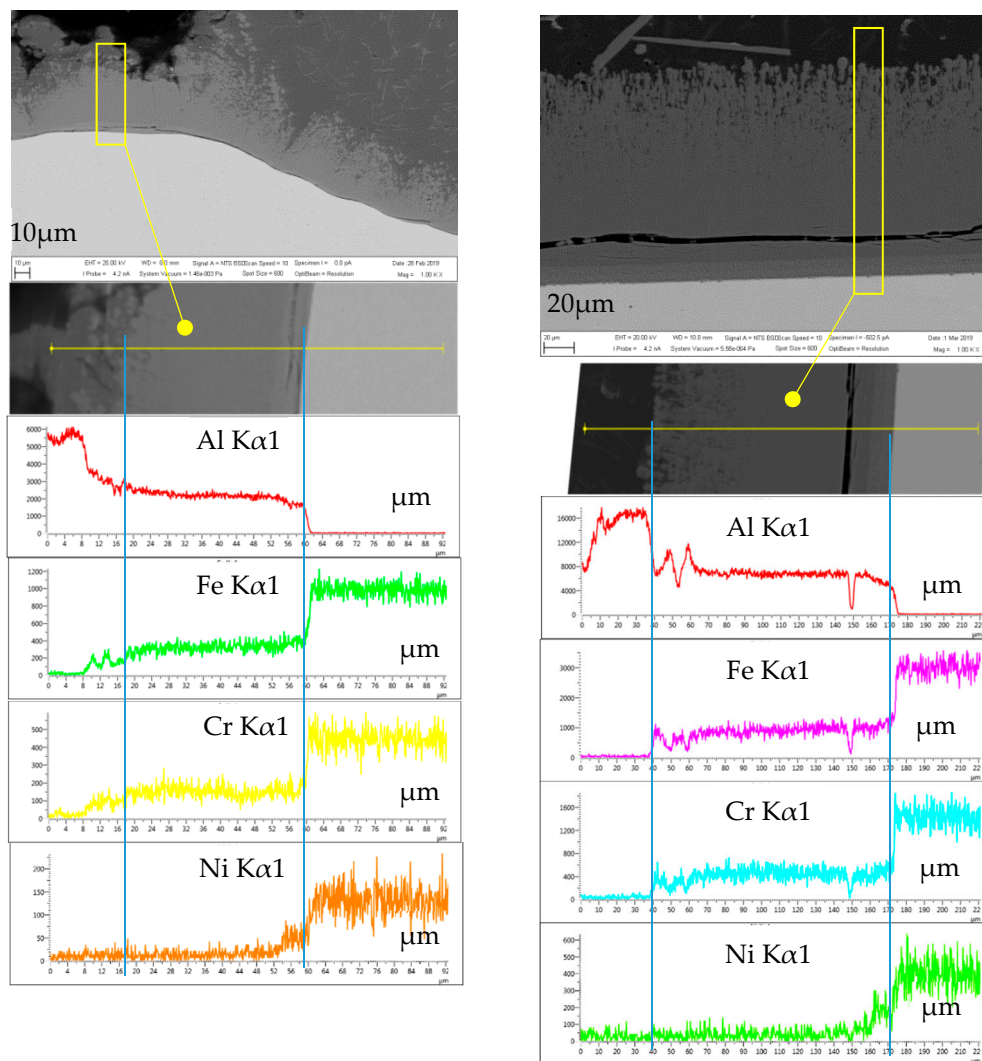


Figure 22. EDX line microanalysis.

3.2.3. Immersion Test of the Base Material

Immersion tests of 18Cr-10Ni stainless steel (BM) in the melt of the ENAC- AlSi9 alloy at $680 \pm 20 \text{ }^\circ\text{C}$ showed that the dissolution process was non-selective and diffusion-driven. After immersion times of 120 and 300 min, it was determined that, between the steel BM and the melt, two intermetallic layers were formed at a temperature of $680 \pm 20 \text{ }^\circ\text{C}$ (Figure 23).

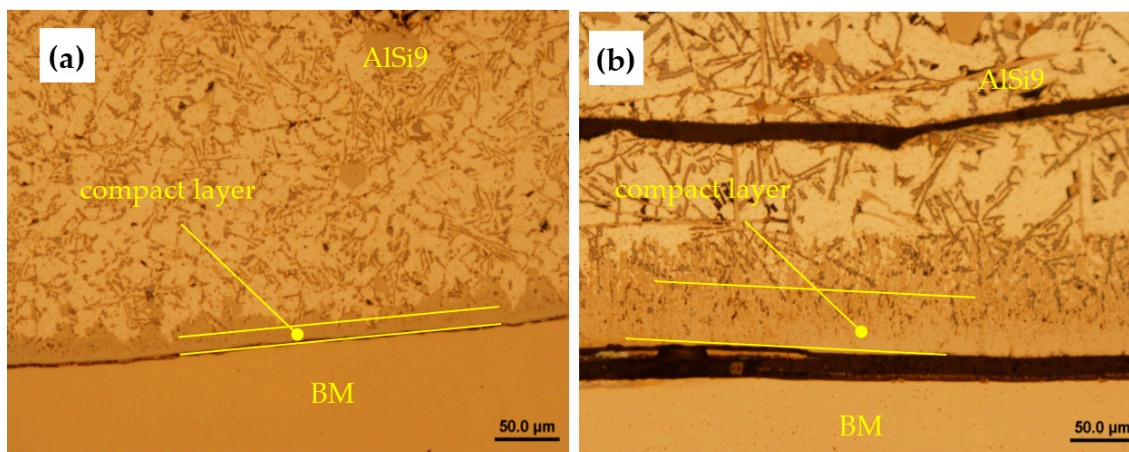


Figure 23. Intermetallic compounds at boundary between BM and solidified aluminum alloy melt after immersion: (a) $680 \pm 20 \text{ }^\circ\text{C}/120 \text{ min}/\text{AlSi9}$, (b) $680 \pm 20 \text{ }^\circ\text{C}/300 \text{ min}/\text{AlSi9}$.

The compact layer adjacent to the steel surface of BM steel consists of iron- and aluminum-based compounds (Table 11, Figure 24). A layer consists of insulated blocks of corrosion products in the liquid part of the ENAC- AlSi9 melt after solidification. Temporary joints between the BM steel and the solidified ENAC- AlSi9 melt were formed by the interaction of a solid steel base material with the liquid aluminum alloy melt.

Table 11. BM/ $680 \pm 20 \text{ }^\circ\text{C}/120 \text{ min}/\text{ENAC-}\text{AlSi9}$. EDX semi-quantitative microanalyses.

Spectrum 1	Spectrum 1		Spectrum 2	
	Element	Weight%	Element	Weight%
	O	0.62	Al	58.91
	Al	82.6	Si	9.68
	Si	15.28	Cr	7.92
	Fe	0.58	Mn	1
	Ni	0.92	Fe	21.87
	-	-	Ni	0.62
	Totals	100.00	Totals	100

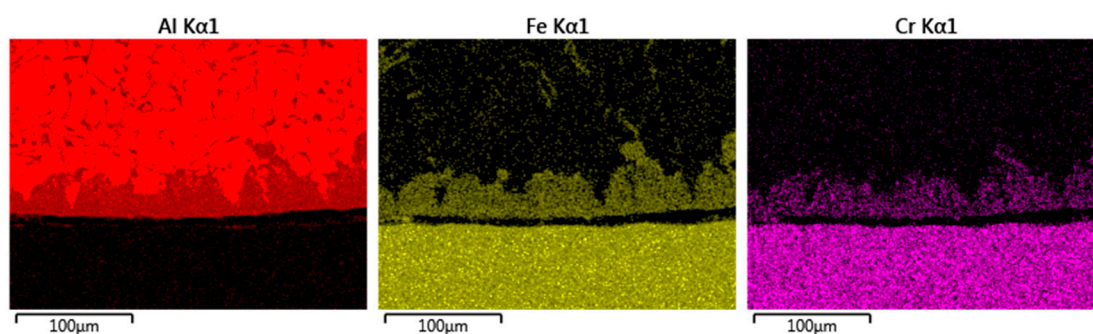
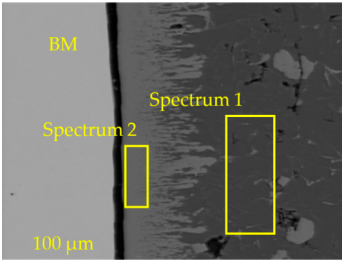


Figure 24. BM/ $680 \pm 20 \text{ }^\circ\text{C}/120 \text{ min}/\text{ENAC-}\text{AlSi9}$. EDX semi-quantitative microanalyses (mapping).

Consistent with [39–46], it was found that the resistance of stainless steel BM in an ENAC-AlSi9 melt at 680 ± 20 °C tested by the immersion technique was a diffusion-controlled non-selective dissolution process.

Results of the EDX semi-quantitative analysis together with EDX line microanalysis of the layer formed on the surface of base material after 300 min of immersion in melt are shown in Table 12 and Figure 25.

Table 12. BM/ 680 ± 20 °C/300 min/ENAC-AlSi9. EDX semi-quantitative microanalyses.

	Spectrum 1		Spectrum 2	
	Element	Weight%	Element	Weight%
	Al	84.36	Al	59.16
	Si	15.09	Si	9.55
	Ni	0.55	Cr	7.94
	Totals	100	Mn	0.99
	-	-	Fe	22.36
	-	-	Totals	100

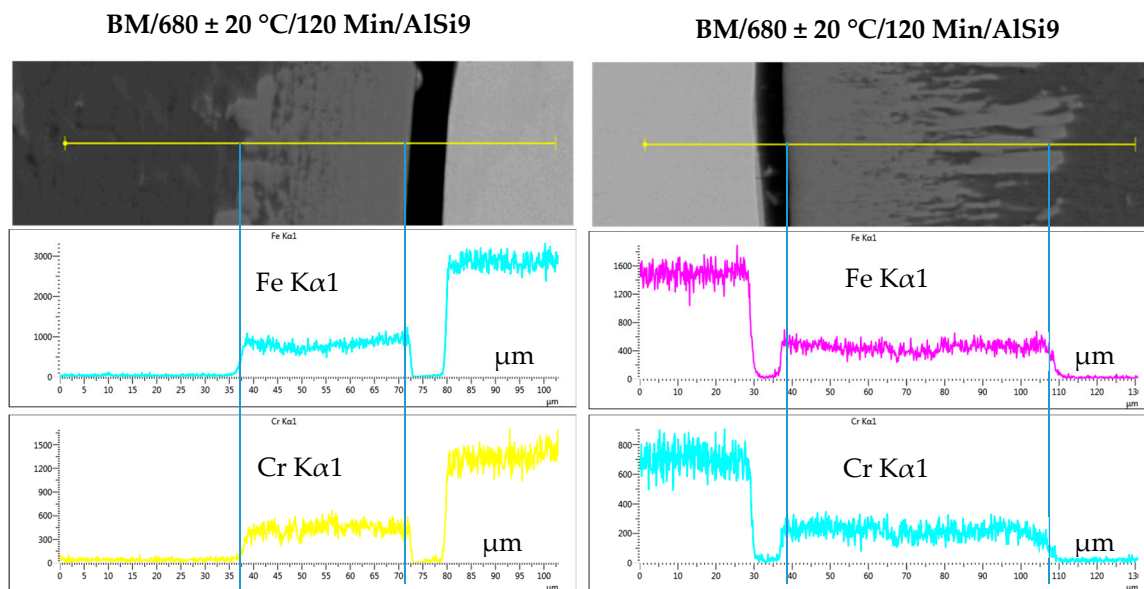


Figure 25. EDX line microanalysis.

The layers formed on the surface of chromium-nickel austenitic steel (BM) consisted of two areas: the top aluminum layer and the aluminide layer at the boundary between Cr-Ni steel and the solidified melt of the ENAC-AlSi9 alloy. The top aluminum layer consisted of intermetallic phases, based on Al-Cr and Al-Fe dispersed in an aluminum matrix. Analogous microstructures of layers formed on the surface of chromium-nickel austenitic steel after exposure to aluminum melt have been observed in several works [39–41].

3.3. Measurement of Compact Layer Thickness

The aim of analyses of the compact layer on the boundary of weld deposit and corrosion products coming from melt/welded clad reaction was to identify the thickness of the corrosion products that would be suitable for qualitative assessment of weld resistance to corrosion dissolution in the melt of aluminum alloy ENAC-AlSi9. These are tests of corrosion resistance of welded clads in the melt of aluminum alloy ENAC-AlSi9 carried out on test specimens manufactured in such a way that the weld clad and the base material are tested simultaneously. For the purposes of this research, we have defined a compact layer as an area with a qualitatively even distribution of those weld deposit elements that

have reacted intensively with the aluminum alloy melt ENAC- AlSi9 . The thickness of this compact layer, measured on a series of cross-sections by light microscopy was used as a criterion for assessing the corrosion resistance of weld deposits in the ENAC- AlSi9 aluminum alloy melt. Separated blocks of corrosion products in the liquid part of the melt after solidification were not included in the corrosion resistance evaluation in this method. The reason was the high heterogeneity in the distribution of corrosion products in the liquid part of the aluminum alloy after its solidification. The idea of assessing the thickness of the compact layer was the result of an effort to propose a simple method for qualitatively assessing the relative corrosion resistance of the welded clads against to the base material in the aluminum alloy melt. For these reasons, the analyses were focused only on the compact layer of corrosion products at the welded clad/solidified melt boundary. The ratio of the thickness of the compact intermetallic layer formed on the base material and welded clad was used as a criterion of corrosion resistance assessment in the melt of the aluminum alloy ENAC- AlSi9 . Measurement of the thickness of the compact layer of the individual welded clads and base material was performed by light microscopy technique on metallographic cross-sections. The number of thickness measurement was approximately 400 for each weld deposit exposed in the ENAC- AlSi9 aluminum alloy melt for 120 min and 300 min (Table 13, Figure 26).

Table 13. Thickness of compact intermetallic layer (μm).

Statistic Parameters	Immersion 120 Min			Immersion 300 Min		
	BM	E 18 8 Mn B 2 2	E Ni 6625	BM	E 18 8 Mn B 2 2	E Ni 6625
Average	20	39	186	28	131	442
StDev	7.4	17.4	7.4	34	34	43
Max	35	80	200	160	160	500
Min	10	18	150	52	52	350

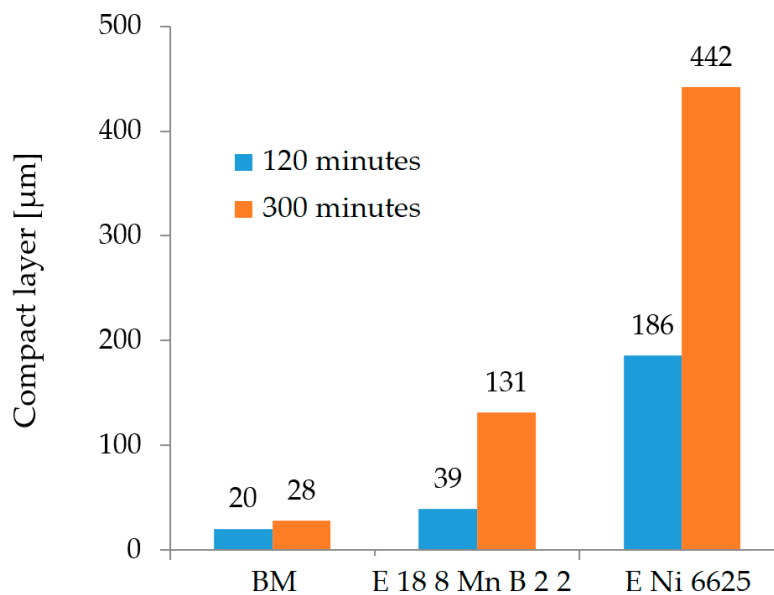


Figure 26. Compact layer thickness.

It can be seen from Figure 26 that the compact layer thickness resulting from the dissolution of the weld deposit was greater than the layer thickness formed on the base material. The layer of intermetallic compounds on the E Ni 6625 surface reached three times the thickness of the E 18 8 Mn B 2 2 surfacing product layer. The ratio of the intermetallic layer thickness formed on base material to that one formed on welded clad was used as a criterion of corrosion resistance against dissolution in the melt of the aluminum alloy ENAC- AlSi9 (Figure 27).

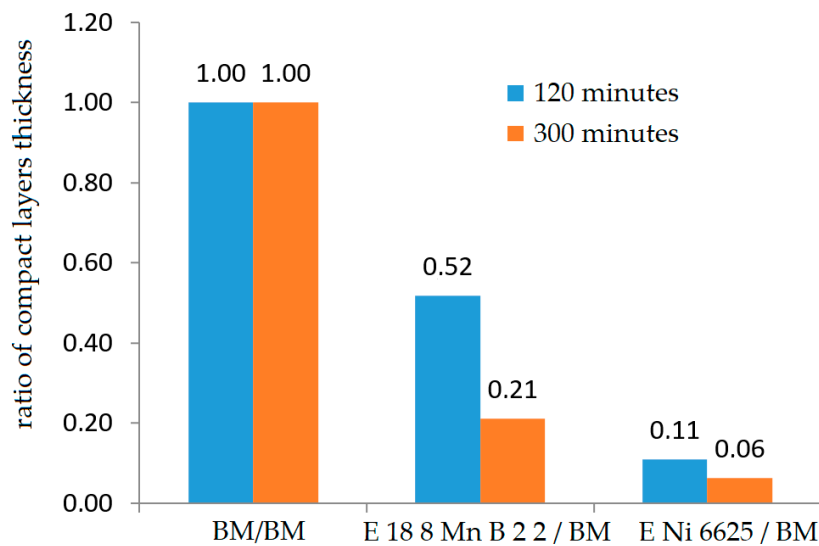


Figure 27. Relative corrosion resistance of welded clads to the base material.

Relative corrosion resistance of cladding corresponds to their thickness. The E Ni 6625 and E 18 8 Mn B 2 2 welded clads have lower weld resistance than the base material. The intense reaction of aluminum melt with E Ni 6625 melt was observed on the samples (Figures 13 and 15). The resistance of E 18 8 Mn B 2 2 weld (Figures 18 and 20) and BM in the aluminum alloy melt (Figures 23 and 26) was higher than the resistance of E Ni 6625 weld. During the 120 and 300 min exposures of E Ni 6625 weld in the aluminum alloy melt a complex reaction of aluminum alloy EN AB ENAC- AlSi9 with alloying elements present in the welds was observed. Using the qualitative elemental EDX microanalysis on the surface of the E Ni 6625 weld individual complex phases based on chromium, nickel, iron, molybdenum and niobium were observed (Tables 7 and 8, Figures 14, 16 and 17). After the 120 and 300 min exposures of E 18 8 Mn B 2 2 welds in the aluminum alloy melt a lower intensity of a reaction of aluminum alloy EN AB ENAC- AlSi9 with the alloying elements present in the welds was observed in the layer of solid aluminum alloy. Using the qualitative elemental EDX microanalysis on the surface of the E 18 8 Mn B 2 2 weld individual complex phases based on chromium, manganese, nickel and iron were observed (Tables 9 and 10, Figures 19, 21 and 22).

4. Conclusions

This paper presents the results of the research focused on the possibility of the renovation of shape parts of mold in the technology of aluminum casting under high pressure. The quality of two weld types—E Ni 6625 and E 18 8 Mn B 2 2—in aluminum alloy melt EN AB ENAC- AlSi9 was determined experimentally. For the production of welds the technology of CMT welding in a protective atmosphere of Ar was used.

The welds used for mold renovation are complexly loaded—mechanically (erosion, abrasion), chemically (high-temperature corrosion) and thermally (thermal shocks). The interaction between the weld and the processed melt is a complex process. The results of this process reflect the superposition the mutual chemical reactions, the specific mechanical, chemical and physical properties of the weld, its ability to resist wear and oxidation, to compensate for the thermal and residual stresses generated by the HPDC process and to delay the onset of thermal fatigue. Moreover, during the life cycle of the die, the dominant degradation mechanism changes, the individual degradative factors interact, and their significance and intensity change over time. To study this complex problem is experimentally challenging. That is why the authors have focused on studying the resistance against dissolution in molten metal.

Samples were exposed to the aluminum alloy melt for 120 and 300 min. The EDX microanalyses of element distribution were performed at the welding interface.

Experimental work confirmed that after 120 and 300 min exposure of E Ni 6625 welds in aluminum alloy melt, a complex reaction of aluminum alloy EN AB ENAC- AlSi9 with alloying elements present in the welds was observed. Using the qualitative elemental microanalysis EDX on the surface of the E Ni 6625 and E 18 8 Mn B 2 2 welded clads individual complex phases based on chromium, nickel, iron, molybdenum and niobium were detected as a result of reaction between them and molten aluminum metal. An intense reaction of the aluminum melt with the E Ni 6625 weld occurred. Resistance of the E 18 8 Mn B 2 2 weld and the underlying material BM in the aluminum alloy melt was higher than the resistance of the E Ni 6625 weld.

The resistance of welded clads in molten aluminum alloy EN AB ENAC- AlSi9 is a superposition of several processes, the intensity of which varies during exposition of welded clads and base material in the melt. The different corrosion resistance of welded clads in the EN AB ENAC- AlSi9 melt is determined by the different chemical concepts of the weld deposits. Welding wire E Ni 6625 was Ni-based and wire E 108 8 Mn B 2 2 was Fe-based. Processes of the interaction in the melt generally consist of dissolution reactions at the clad-melt boundary, mass transfer to the melt or mass transfer from the melt to clad-melt boundary and the precipitation and recrystallization processes. These processes take place continuously on the surface of the base material and welded clads and under the same experimental conditions. Such an experimental arrangement makes it possible to effectively evaluate the relative resistance of the materials used for the renovation of molds against dissolution in the melt compared to the original mold material. The resistance of the materials used for mold renovation should not be less than that of the original mold material.

Based on the experiments carried out it can be stated that the evaluated types of welds are not suitable for the renovation of the shape parts of molds because the elements are dissolved in contact with the aluminum alloy. For this type of renovation a combination of welds and duplex PVD coating can be recommended.

Author Contributions: Supervision: J.B. (Janette Brezinová); writing—original draft preparation: M.D.; investigation: M.V.; methodology: J.B. (Jakub Brezina); validation: O.M.; resources: J.V.; writing—review and editing: A.G., D.D.

Funding: This contribution is the result of the project implementation: The utilization of innovative technology for the repair of functional surfaces of mold casting dies for castings in automotive industry (APVV-16-0359) supported by the Slovak Research and Development Agency and Study of the properties of newly constituted layers and coatings in tribological systems (VEGA 1/0424/17).

Conflicts of Interest: The authors declare no conflict of interest.

References

1. Hirsch, J. Recent development in aluminium for automotive applications. *Trans. Nonferr. Met. Soc. China* **2014**, *24*, 1995–2002. [[CrossRef](#)]
2. Pickin, C.G.; Williams, S.W.; Lunt, M. Characterisation of the cold metal transfer (CMT) process and its application for low dilution cladding. *J. Mater. Process. Technol.* **2011**, *211*, 496–502. [[CrossRef](#)]
3. Jhavar, S.; Paul, C.P.; Jain, N.K. Causes of failure and repairing options for dies and molds: A review. *Eng. Fail. Anal.* **2013**, *34*, 519–535. [[CrossRef](#)]
4. Chander, S.; Chawla, V. Failure of hot forging dies—An updated perspective. *Mater. Today Proc.* **2017**, *4*, 1147–1157. [[CrossRef](#)]
5. Chen, C.; Wang, Y.; Ou, H.; He, Y.; Tang, X. A review on remanufacture of dies and moulds. *J. Clean. Prod.* **2014**, *64*, 13–23. [[CrossRef](#)]
6. Taylan, A.; Blaine, L.; Yen, Y.C. Manufacturing of dies and molds. *CIRP Ann.* **2001**, *50*, 404–422. [[CrossRef](#)]
7. Lin, J.; Carrera, S.; Kunrath, A.O.; Zhong, D.; Myers, S.; Mishra, B.; Ried, P.; Moore, J.J. Design methodology for optimized die coatings: The case for aluminum pressure die-casting. *Surf. Coat. Technol.* **2006**, *201*, 2930–2941. [[CrossRef](#)]
8. Joshi, V.; Srivastava, A.; Shivpuri, R.; Rolinski, E. Investigating ion nitriding for the reduction of dissolution and soldering in die-casting shot sleeves. *Surf. Coat. Technol.* **2003**, *163–164*, 668–673. [[CrossRef](#)]

9. Psyllaki, P.; Kefalonikas, G.; Pantazopoulos, G.; Antoniou, S.; Sideris, J. Microstructure and tribological behaviour of liquid nitrocarburised tool steels. *Surf. Coat. Technol.* **2002**, *162*, 67–78. [[CrossRef](#)]
10. Suarez, S.A.; Suarez, A.M.; Preciado, W.T. Arc welding procedures on steels for molds and dies. *Procedia Eng.* **2015**, *100*, 584–591. [[CrossRef](#)]
11. Xu, X.; Mi, G.; Xiong, L.; Jiang, P.; Shao, X.; Wang, C. Morphologies, microstructures and properties of TiC particle reinforced Inconel 625 coatings obtained by laser cladding with wire. *J. Alloy. Compd.* **2018**, *740*, 16–27. [[CrossRef](#)]
12. Prakash, K.; Santanu, P.; Ramesh, S.; Wenyi, Y. Experimental characterization of laser cladding of CPM 9V on H13 tool steel for die repair applications. *J. Manuf. Process.* **2015**, *20*, 492–499. [[CrossRef](#)]
13. Santanu, P.; Ramesh, S.; Wenyi, Y. Thermal model for additive restoration of mold steels using crucible steel. *J. Manuf. Process.* **2016**, *24*, 346–354. [[CrossRef](#)]
14. Santanu, P.; Khushahal, T.; Ramesh, S.; Indradev, S.; Wenyi, Y. Experimental characterization of clad microstructure and its correlation with residual stresses. *Procedia Manuf.* **2017**, *10*, 804–818. [[CrossRef](#)]
15. Imoudu, N.E.; Ayele, Y.Z.; Barabadi, A. The characteristic of cold metal transfer (CMT) and its application for cladding. In Proceedings of the International Conference on Industrial Engineering and Engineering Management IEEM, Singapore, 10–13 December 2017; pp. 1883–1887.
16. Pisu, T.M.; Vas, A.; Magyari, M.; Iordache, A. Research on cladding (CMTMIG, WIG arc mechanized pulse) for molds used for casting. *Metal. Int.* **2013**, *18*, 89–94.
17. Chen, M.; Zhang, D.; Wu, C. Current waveform effects on CMT welding of mild steel. *J. Mater. Process. Technol.* **2017**, *243*, 395–404. [[CrossRef](#)]
18. Pang, J.; Hu, S.; Shen, J.; Wang, P.; Liang, Y. Arc characteristics and metal transfer behavior of CMT + P welding process. *J. Mater. Process. Technol.* **2016**, *238*, 212–217. [[CrossRef](#)]
19. Selvi, S.; Vishvakshenan, A.; Rajasekar, E. Cold metal transfer (CMT) technology—An overview. *Def. Technol.* **2018**, *14*, 28–44. [[CrossRef](#)]
20. Gungor, B.; Kaluc, E.; Taban, E.; Sik, A. Mechanical and microstructural properties of robotic COLD METAL TRANSFER (CMT) welded 5083-H111 and 6082-T651 aluminum alloys. *Mater. Des.* **2014**, *54*, 207–211. [[CrossRef](#)]
21. Cong, B.; Ouyang, R.; Qi, B.; Ding, J. Influence of cold metal transfer process and its heat input on weld bead geometry and porosity of aluminum-copper alloy welds. *Rare Met. Mater. Eng.* **2016**, *45*, 606–611. [[CrossRef](#)]
22. Liang, Y.; Shen, J.; Hu, S.; Wang, H.; Pang, J. Effect of TIG current on microstructural and mechanical properties of 6061-T6 aluminium alloy joints by TIG–CMT hybrid welding. *J. Mater. Process. Technol.* **2018**, *255*, 161–174. [[CrossRef](#)]
23. Sun, Q.J.; Li, J.Z.; Liu, Y.B.; Li, B.P.; Xu, P.W.; Feng, J.C. Microstructural characterization and mechanical properties of Al/Ti joint welded by CMT method—Assisted hybrid magnetic field. *Mater. Des.* **2017**, *116*, 316–324. [[CrossRef](#)]
24. Lutterotti, L.; Bortolotti, M.; Ischia, G.; Lonardelli, I.; Wenk, H.R. Rietveld texture analysis from diffraction images. *Z. Kristallogr. Suppl.* **2007**, *26*, 125–130. [[CrossRef](#)]
25. Satyanarayana, D.V.V.; Prasad, N.E. Nickel-based superalloys. In *Aerospace Materials and Material Technologies*; Prasad, N., Wanhill, R., Eds.; Indian Institute of Metals Series; Springer: Singapore, 2017; pp. 199–228. [[CrossRef](#)]
26. Xing, X.; Di, X.; Wang, B. The effect of post-weld heat treatment temperature on the microstructure of Inconel 625 deposited metal. *J. Alloy. Compd.* **2014**, *593*, 110–116. [[CrossRef](#)]
27. Dupont, J.N.; Lippold, J.C.; Kiser, S.D. *Welding Metallurgy and Weldability of Nickel-Base Alloys*, 1st ed.; John Wiley & Sons, Inc.: Hoboken, NJ, USA, 2009; p. 440. [[CrossRef](#)]
28. Rajani, H.R.Z.; Torkamani, H.; Sharbati, M.; Raygan, S. Corrosion resistance improvement in Gas Tungsten Arc Welded 316L stainless steel joints through controlled preheat treatment. *Mater. Des.* **2012**, *34*, 51–57. [[CrossRef](#)]
29. Lippold, J.C.; Kotecki, D.J. *Welding Metallurgy and Weldability of Stainless Steels*, 1st ed.; John Wiley & Sons, Inc.: Hoboken, NJ, USA, 2005; p. 367.
30. Feng, Y.; Luo, Z.; Liu, Z.; Li, Y.; Luo, Y.; Huang, Y. Keyhole gas tungsten arc welding of AISI 316L stainless steel. *Mater. Des.* **2015**, *85*, 24–31. [[CrossRef](#)]
31. Zhang, J.; Hosemann, P.; Maloy, S. Models of liquid metal corrosion. *J. Nucl. Mater.* **2010**, *404*, 82–96. [[CrossRef](#)]

32. Shankar, V.; Rao, K.B.S.; Mannan, S.L. Microstructure and mechanical properties of Inconel 625 superalloy. *J. Nucl. Mater.* **2001**, *288*, 222–232. [[CrossRef](#)]
33. Reed, R.C. *The Superalloys. Fundamentals and Applications*; Cambridge University Press: New York, NY, USA, 2006; p. 372.
34. Jain, M.; Gupta, S.P. Formation of intermetallic compounds in the Ni–Al–Si ternary system. *Mater. Charact.* **2003**, *51*, 243–257. [[CrossRef](#)]
35. Richter, K.W.; Chandrasekaran, K.; Ipsier, H. The Al–Ni–Si phase diagram. Part II: Phase equilibria between 33.3 and 66.7 at. % Ni. *Intermetallics* **2004**, *12*, 545–554. [[CrossRef](#)]
36. Richter, K.W.; Ipsier, H. The Al–Ni–Si phase diagram between 0 and 33.3 at. % Ni. *Intermetallics* **2003**, *11*, 101–109. [[CrossRef](#)]
37. Chandrasekaran, K.; Richter, K.W.; Ipsier, H. The Al–Ni–Si phase diagram—Part III: Phase equilibria in the nickel rich part. *Intermetallics* **2006**, *14*, 491–497. [[CrossRef](#)]
38. Bouayad, A.; Gerometta, C.; Belkebir, A.; Ambari, A. Kinetic interactions between solid iron and molten aluminium. *Mater. Sci. Eng. A* **2003**, *363*, 53–61. [[CrossRef](#)]
39. Huilgol, P.; Udupa, K.R.; Bhat, K.U. Formation of microstructural features in hot-dip aluminized AISI 321 stainless steel. *Int. J. Miner. Metall. Mater.* **2018**, *25*, 190–198. [[CrossRef](#)]
40. Hu, T.L.; Huang, H.L.; Gan, D.; Lee, T.Y. The microstructure of aluminized type 310 stainless steel. *Surf. Coat. Technol.* **2006**, *201*, 3502–3509. [[CrossRef](#)]
41. Huilgol, P.; Udupa, K.R.; Bhat, K.U. Metastable microstructures at the interface between AISI 321 steel and molten aluminum during hot-dip aluminizing. *Surf. Coat. Technol.* **2018**, *348*, 22–30. [[CrossRef](#)]
42. Dybkov, V.I. Interaction of 18Cr–10Ni stainless steel with liquid aluminium. *J. Mater. Sci.* **1990**, *25*, 3615–3633. [[CrossRef](#)]
43. Dybkov, V.I. Interaction of iron-nickel alloys with liquid aluminium. *J. Mater. Sci.* **1993**, *28*, 6371–6380. [[CrossRef](#)]
44. Dybkov, V.I. Interaction of iron-nickel alloys with liquid aluminium Part II formation of intermetallics. *J. Mater. Sci.* **2000**, *35*, 1729–1736. [[CrossRef](#)]
45. Yan, M.; Fan, Z. Review durability of materials in molten aluminum alloys. *J. Mater. Sci.* **2001**, *36*, 285–295. [[CrossRef](#)]
46. Shin, D.; Lee, J.Y.; Heo, H.; Kang, C.Y. Formation procedure of reaction phases in Al hot dipping process of steel. *Metals* **2018**, *8*, 820. [[CrossRef](#)]



© 2019 by the authors. Licensee MDPI, Basel, Switzerland. This article is an open access article distributed under the terms and conditions of the Creative Commons Attribution (CC BY) license (<http://creativecommons.org/licenses/by/4.0/>).